Korean J. Chem. Eng., 39(2), 343-352 (2022)
DOI: 10.1007/s11814-021-0925-y

pISSN: 0256-1115
eISSN: 1975-7220

Enhanced photocatalytic activity on elemental mercury over pink $BiOIO_3$ nanosheets with abundant oxygen vacancies

Yang Ling*,‡, Jiachen Li,‡, Jiang Wu*,**,†, Hailong Liu**, Xu Mao**, Yongfeng Qi***, Qian Ma**, Qizhen Liu****,†, Zhanwei Qiao**, and Weiqun Chu****

*School of Energy and Power Engineering, University of Shanghai for Science and Technology, Shanghai 200093, China
**College of Energy and Mechanical Engineering, Shanghai University of Electric Power, Shanghai 200090, China
***School of Hydraulic Energy and Power Engineering, Yangzhou University, Yangzhou 225127, China
****Shanghai Environment Monitoring Center, Shanghai 200030, China
(*Received 17 May 2021 • Revised 4 August 2021 • Accepted 12 August 2021*)

Abstract−Elemental mercury removal in coal-fired power plants is the key to global mercury pollution control, and photocatalytic oxidation is an effective and stable method. As a typical bismuth-based photocatalyst, $BiOIO_3$ has a large band gap which is not conducive to the absorption and utilization of visible light, and its specific surface area also limits the diffusion and adsorption of reactants. In this work, pink $BiOIO_3$ (PB) was first prepared successfully via vacuum calcination under absolute pressure of $1*10^{-3}$ Pa. The specific surface area of pink $BiOIO_3$ is significantly increased to 44.52 m^2/g, which is 1.5-times compared with the traditional $BiOIO_3$ prepared by hydrothermal method (only 29.60 m^2/g). Abundant oxygen vacancy defects exist on sample surface, and the formed local BiOI Zero-dimensional (0-D) nanodots provide heterojunction-like effect combined with the $BiOIO_3$, obtaining better photocatalytic property in the oxidation of elemental mercury. The as-prepared pink $BiOIO_3$ and the preparation technology also have strong application potential in the field of energy and environment.

Keywords: Power Plant, Elemental Mercury, $BiOIO_3$, Photocatalysis, DFT

INTRODUCTION

Coal-fired power plants are the largest anthropogenic sources of mercury emissions, and the effective control of flue gas mercury is the key to global mercury pollution control [1]. Although a series of measures have been taken to control the diffusion and volatilization of toxic gases during boiler production, residual pollutants continue to endanger public health and safety. Wet flue gas desulfurization (WFGD) is generally used to remove oxidized mercury, while other mercury particles are adsorbed on particulate carbon and then captured and removed by electrostatic precipitator or wet electrostatic precipitator (ESP/WESP) [2-4]. However, due to its stable chemical properties, elemental mercury (Hg^0) is not easily soluble in water, nor adhere to fly ash, that often exists in the gaseous form, and the emission through the chimney, which is the key scientific issue of mercury emission from power plants [5].

Intra-flue injection adsorption is a common method for mercury removal, and activated carbon is usually used as the adsorption material [6-8]. While, considering the enormous amount of flue gas emissions, the cost of adopting injection method is high, which will also lead to increased power consumption and coal consumption for power generation. In recent years, photocatalytic oxidation of mercury after combustion has been widely studied as a low cost and high efficiency mercury removal method [9]. Conventional titanium dioxide as a photocatalyst has a wide band gap of about 3.2 eV, so its valence band electrons can only be excited by ultraviolet light with a shorter wavelength, and the photogenerated electron-hole pair recombination rate is also high [10]. The main characteristics required for photocatalysts include broadening the spectral response range [11], reducing the recombination rate of photogenerated electrons and holes [12], and increasing their chemical/physical stability [13,14]. As an alternative, bismuth-based materials have been extensively studied by researchers due to their unique layered structure, photocatalytic activity and good chemical stability [15-18], which are potential photocatalytic mercury removal agents [19].

$BiOIO_3$, a typical bismuth-based semiconductor photocatalyst, with double lone-pair cations in the $(Bi_2O_2)^{2+}$ and $(IO_3)^-$ Aurivillius layered structure, has excellent macroscopic polarity characteristics [20]. It is often used in many energy and environmental fields such as artificial photosynthesis [21], denitrification [22], hydrogen production [23], organic degradation [24], and demercuration [25]. The valence band (VB) position of $BiOIO_3$ is so positive [26] that the photogenerated holes enriched in the VB lead to extremely strong oxidation performance, and the internal electric field formed by the IO_3 polyhedra alignment is advantageous to the separation of photo-generated carriers. However, pure $BiOIO_3$ has relatively large band gap which inhibits the utilization of visible light, and small specific surface area that is not conducive to the diffusion and adsorption of reactants, hence there is still much room for improvement.

†To whom correspondence should be addressed.
E-mail: wjcfd2002@163.com, liuqz@sheemc.cn
‡Yang Ling and Jiachen Li have equal contribution to this work.
Copyright by The Korean Institute of Chemical Engineers.

In this work, pure $BiOIO_3$ nanosheets were treated by vacuum calcination, and a new type pure substance phase, Pink $BiOIO_3$ (PB), was successfully synthesized. It has increased specific surface area and abundant surface oxygen vacancy defects, and the efficiency of elemental mercury photocatalytic oxidation was significantly improved. Meanwhile, the related mechanism of photocatalytic performance improvement has also been analyzed via density functional theory.

EXPERIMENTAL

1. Preparation

First, the pure $BiOIO_3$ was prepared via traditional hydrothermal method as follows [27]. In a typical reaction, 5 mmol $Bi(NO_3)_3 \cdot 5H_2O$ was added to a beaker containing 80 mL deionized water and 4 mL 67% (w/w) HNO_3, followed by constant stirring for 10 min. Then, 5 mmol KIO_3 was added to the above beaker and constant stirring for another 30 min. The mixture was transferred into a 100 mL Teflon-lined stainless autoclave for hydrothermal process at 160 °C and lasted 12 h (heating rate 5 °C/min). The product was centrifugally washed with deionized water and absolute ethyl alcohol, respectively, for three times and then dried at 80 °C for 12 h. The pure $BiOIO_3$ nanosheets prepared via hydrothermal were labeled as $BiOIO_3$-H (H for hydrothermal).

The pink $BiOIO_3$ (PB) was obtained via vacuum calcination of pure $BiOIO_3$ nanosheets (Fig. 1). In a typical procedure, 0.4 g of the above as-prepared samples was put it into the bottom of a quartz tube (12 mm of inner diameter, 200 mm of length). A small piece of quartz was placed in the middle of the quartz tube. The inner space of the quartz tube was gradually vacuumed by molecular pump, with the absolute pressure of $1*10^{-3}$ Pa. The mixture of hydrogen and oxygen was ignited to obtain a steady and violent premixed flame. Immediately, the hot outer flame was aimed at the quartz piece, producing a bright white flare until it was melted and became an entirety with the surrounding quartz wall. The vacuum

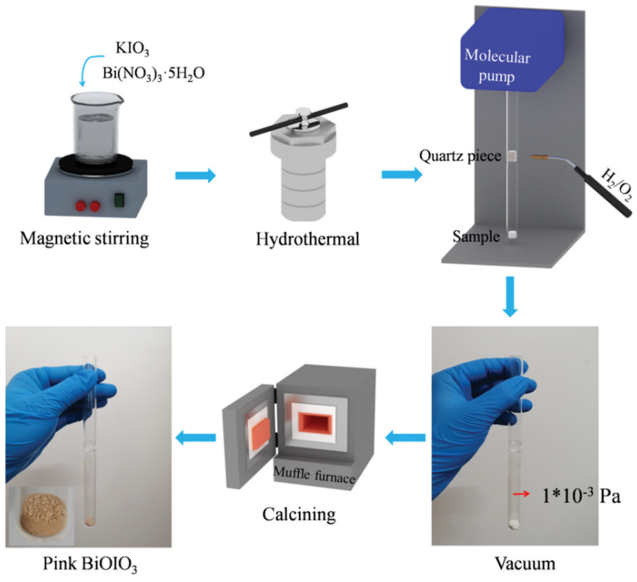

Fig. 1. Preparation process of the pink $BiOIO_3$.

treated quartz tube was transferred to muffle furnace and calcined at 200 °C for 2 h (heating rate 10 °C/min), while the setting of this temperature was referred to our previous work [28]. Finally, the quartz tube was naturally cooled to room temperature and the prepared pink $BiOIO_3$ was obtained (labeled as $BiOIO_3$-VC, VC for vacuum calcination). To verify the necessity of vacuum environment, a control sample was prepared. The pure $BiOIO_3$ prepared via hydrothermal method ($BiOIO_3$-H) was calcined directly in a muffle furnace (keeping the other parameters unchanged), and the obtained control samples was labeled as $BiOIO_3$-C (C for calcination).

2. Characterization

The as-prepared samples were characterized by XRD (Bruker D8 Advance, Germany), BET (Micromeritics ASAP 2020), SEM (Phillips XL-30 FEG/NEW), XPS (PHI5300, USA) and UV-vis DRS (SHIMADZU UV-3600, Japan).

3. Evaluation of Photocatalytic Performance

The as-prepared samples were evaluated by photocatalytic oxidation of gaseous elemental mercury (Hg^0), of which effective control is considered to be the key of the total mercury control in coal-fired flue gas. The experimental setup is similar to before [29] and the details are described in the Supplementary Material (Fig. S1).

4. Density Functional Theory Calculation Details

The density functional theory (DFT) calculation in this paper was carried out via CASTEP code. The exchange-correlation functional used the Perdew-Burke-Ernzerhof (PBE) functional under the generalized gradient approximation (GGA) [30]. The convergence criteria for self-consistent field iterative calculation were: maximum energy change of 2.0×10^{-5} eV/atom, maximum force of 0.05 eV/Å, maximum stress 0.1 GPa, and maximum displacement 0.002 Å. In each calculation, geometric optimization was first carried out for the constructed model. Then, the energy, band structure, density of states and optical properties were calculated on the basis of geometrically optimized structure.

RESULTS AND DISCUSSION

From Fig. 2(a), the XRD patterns show that the three samples are all pure phase $BiOIO_3$ (ICSD #262019 [31]), indicating the successful preparation of pink $BiOIO_3$. Although BiOI is brick red, there is no characteristic peak about it, which means the bulk BiOI crystal does not form during the vacuum calcination progress. It is not bulk BiOI that caused the sample to turn pink color but other reasons. The characteristic crystal surfaces of $BiOIO_3$-VC: (010) and (121) facets became more sharp, which is due to the vacuum environment isolated from the interference of external impurities. Under heating conditions, the crystallinity of $BiOIO_3$ is significantly increased, and the exposure of (010) facets active surface is enhanced [32]. In comparison, the peak value of (010) facets (with better reactivity efficiency) in $BiOIO_3$-C is significantly shorter, showing the reduction in crystallinity and the crystal structure was destroyed in the calcination process.

From Fig. 2(b) and Table 1, the specific surface area of $BiOIO_3$-VC is significantly enhanced, reaching 44.52 m^2/g, which is 1.5-times of $BiOIO_3$-H (29.60 m^2/g). Due to the influence of vacuum environment, the adsorbed gas on the surface and inside of the sample is desorbed, which makes the sample more fluffy. This also

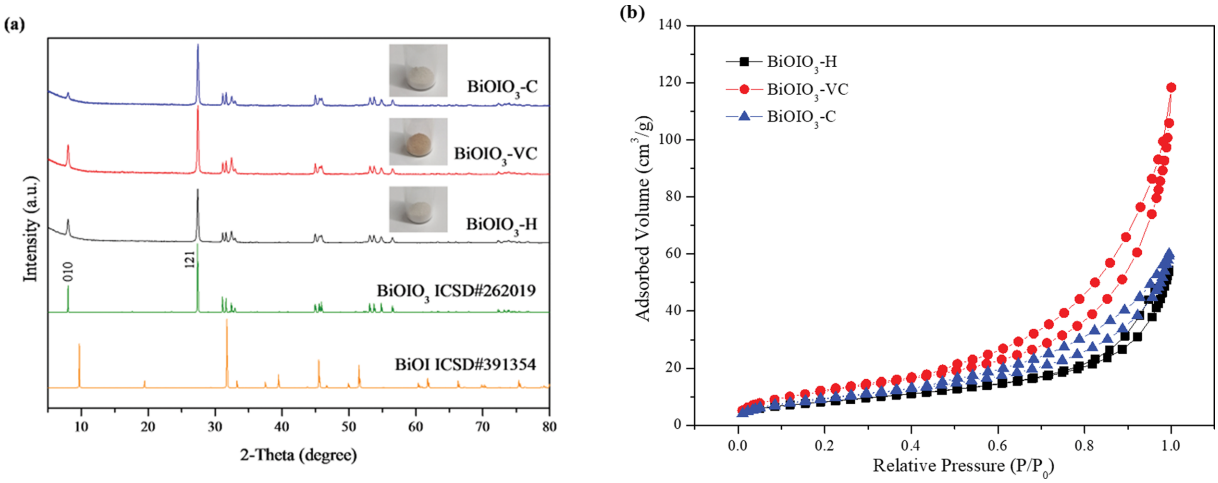

Fig. 2. (a) XRD patterns; (b) N_2 adsorption-desorption isotherms and corresponding data.

Table 1. Summary of physical and photocatalytic properties

Samples	BET surface area m^2/g	Total pore volume cm^3/g	Average pore diameter nm	Adsorbing boundary nm	Bandgap eV	Hg^0 removal efficiency %
$BiOIO_3$-H	29.60	0.0788	10.65	415	2.99	58
$BiOIO_3$-VC	44.52	0.1510	13.57	441	2.81	78
$BiOIO_3$-C	34.44	0.0874	10.16	416	2.98	60

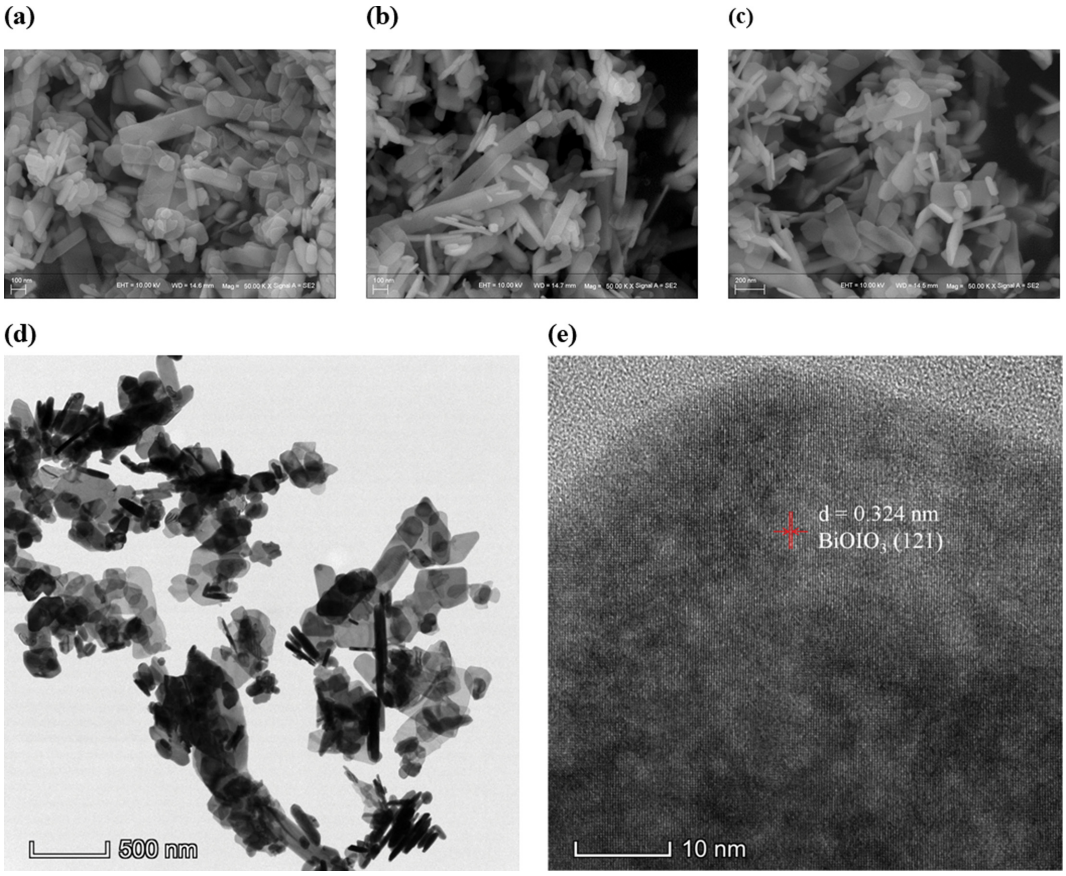

Fig. 3. SEM images for (a) $BiOIO_3$-H, (b) $BiOIO_3$-VC and (c) $BiOIO_3$-C; (d) TEM image of $BiOIO_3$-VC; (e) HR-TEM image of $BiOIO_3$-VC.

resulted in the rich total pore volume (0.1510 cm^3/g) and larger average pore diameter (13.57 nm), which are significantly increased compared with the other two samples. That is beneficial to the adsorption of reactants, such as mercury atoms, which is also consistent with the experimental conclusion.

The $BiOIO_3$-H prepared by hydrothermal method shows typical nanosheet structure (Fig. 3(a)), which is well consistent with the literature [27]. The morphology of $BiOIO_3$-VC (Fig. 3(b)) is similar to that of $BiOIO_3$-H, with sharp edges in nanosheets. It can be found that vacuum calcination changes the spatial layout of $BiOIO_3$ nanosheets: the agglomeration of samples is reduced, forming more fluffy and porous three-dimensional structure, while the abundant pores are beneficial to the internal diffusion and adsorption of reactants. The $BiOIO_3$-C nanosheets become rougher and the sharp edges gradually disappear (Fig. 3(c)), which is in line with the XRD analysis. From the TEM and HR-TEM image of $BiOIO_3$-VC (Fig. 3(d) and (e)), the sample shows an irregular lamellar structure, and clear latice fringes of 0.324 nm can be observed, corresponding to the diffraction of $BiOIO_3$ (121) plane [33]. While no lattice fringes of BiOI appear, because the BiOI is locally generated and no large chunks of BiOI crystal present, which is also consistent well with the XRD analysis above.

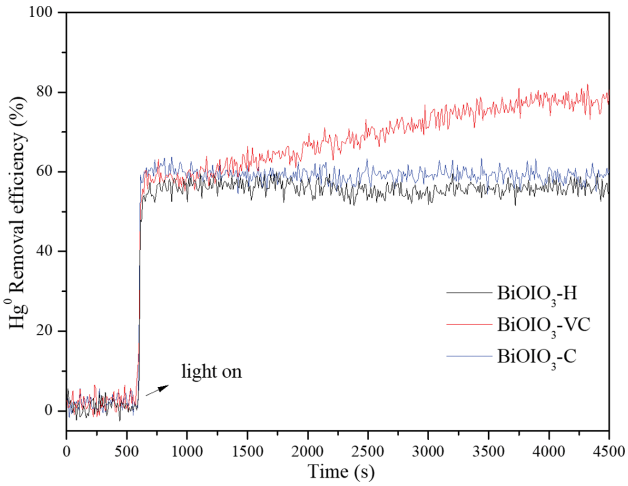

Fig. 4. Elemental mercury removal efficiency of the as-prepared samples.

The photocatalytic performance of the three as-prepared samples

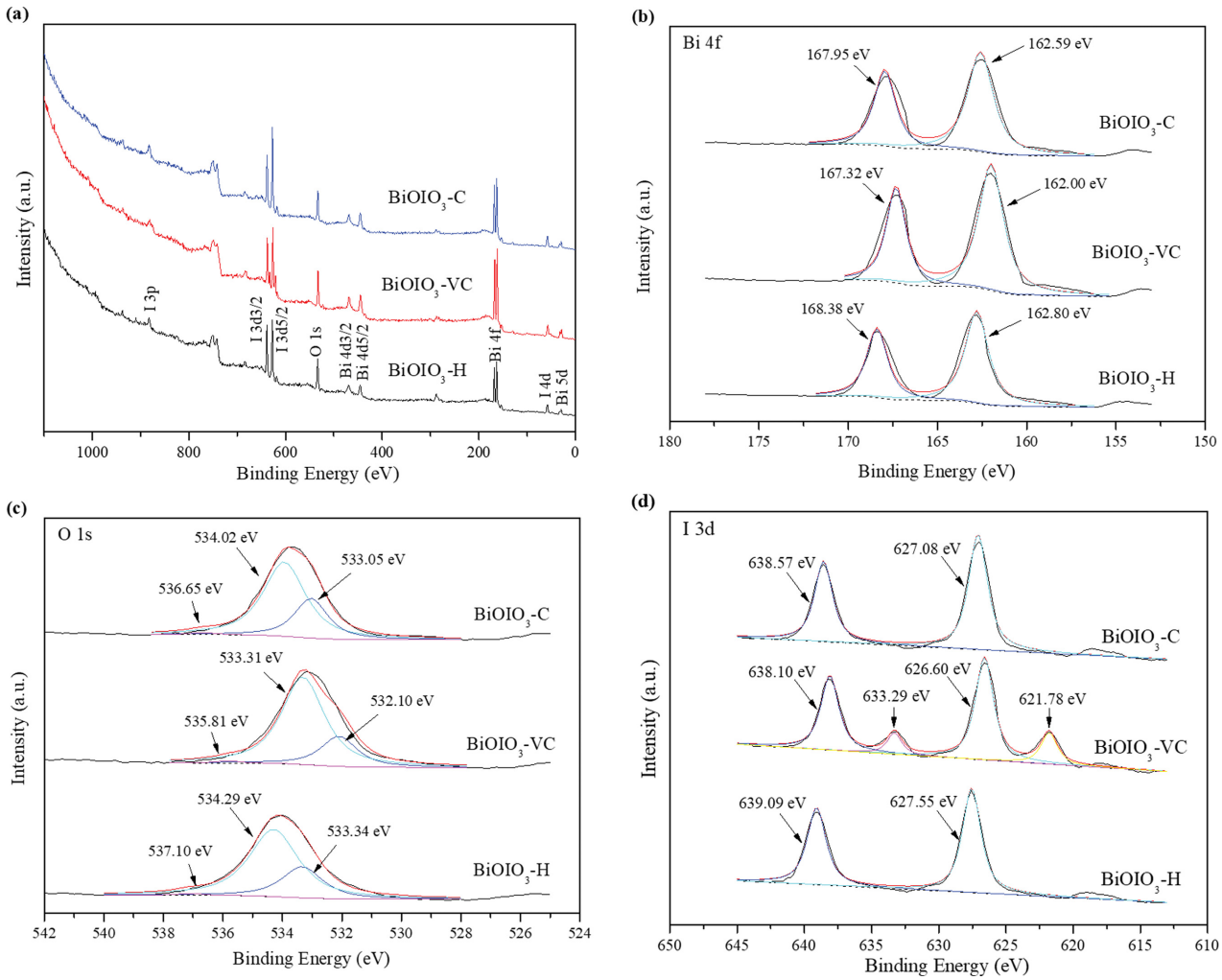

Fig. 5. (a) Fully survey scanned XPS spectra; High resolution XPS spectra for (b) Bi 4f, (c) O 1s and (d) I 3d.

was evaluated by the photocatalytic oxidation of elemental mercury (Hg^0) under visible light irradiation (with the filter λ>400 nm), and the results are shown in Fig. 4 and Table 1. The Hg^0 removal efficiency of $BiOIO_3$-H was only 58%, because of the large band gap (~3 eV), which is not conducive to the utilization of visible light, and the weak specific surface area and pore structure hindered the adsorption of reactants. In contrast, the efficiency of $BiOIO_3$-VC was significantly improved, reaching 78%, which is 39% higher than $BiOIO_3$-H. The efficiency of $BiOIO_3$-C was about 60%, which was not significantly changed and almost the same as that of $BiOIO_3$-H, indicating the necessity of vacuum calcination for the formation of the pink $BiOIO_3$.

Next, the mechanism of improving the photocatalytic performance of the pink $BiOIO_3$ prepared by vacuum calcination was further explored. The XPS spectra of the as-prepared samples are shown in Fig. 5. The element shown in the full spectrum (Fig. 5(a)) is well consistent with the chemical composition of the sample. Fig. 5(b) is the high-resolution spectrum of the Bi 4f, and two obvious peaks at 162.00-162.80 and 167.32-168.38 eV can be attributed to the contribution of Bi $4f_{7/2}$ and Bi $4f_{5/2}$, respectively [34]. The valence state change of bismuth element is not obvious, because the bismuth atom is located in the $(Bi_2O_2)^{2+}$ skeleton of the $BiOIO_3$ crystal, and the chemical environment is relatively stable. Fig. 5(c) is XPS spectrum of O 1s. The two main peaks come from two different forms of oxygen: the peaks in the range of 532.10-533.34 eV are the oxygen in $(Bi_2O_2)^{2+}$ layer, while the peaks in the range of 533.31-534.29 eV are the oxygen in $(IO_3)^-$ [28]. There are also some small peaks appearing at around 535.81-537.10 eV, which are caused by the adsorption of water and hydroxyl groups on the sample surface [35]. From the XPS spectrum of I 3d (Fig. 5(d)), the $BiOIO_3$-C is similar to $BiOIO_3$-H, that both have peaks within 627.08-627.55 eV and 638.57-639.09 eV, corresponding to the contribution of I^{+5} in the $(IO_3)^-$ layer [36]. However, the $BiOIO_3$-VC not only has I^{+5} peaks, but also produces an obvious pair of I^{-1} peaks in 621.78 eV and 633.29 eV. This can be attributed to the induction of vacuum calcination, resulting in the formation of oxygen vacancies on the sample surface. In addition, the surface $(IO_3)^-$ layers lose some surface oxygen atoms, thus forming local BiOI Zero-dimensional (0-D) nanodots, which causes heterojunction-like effect with $BiOIO_3$. While reducing the band gap, the photocatalytic activity of the pink $BiOIO_3$ is improved relying on type-II heterojunction. Since the oxygen atoms on $BiOIO_3$ nanosheets surface are lost uniformly and do not form bulks of BiOI crystal, there is no characteristic peak of BiOI observed in the XRD pattern.

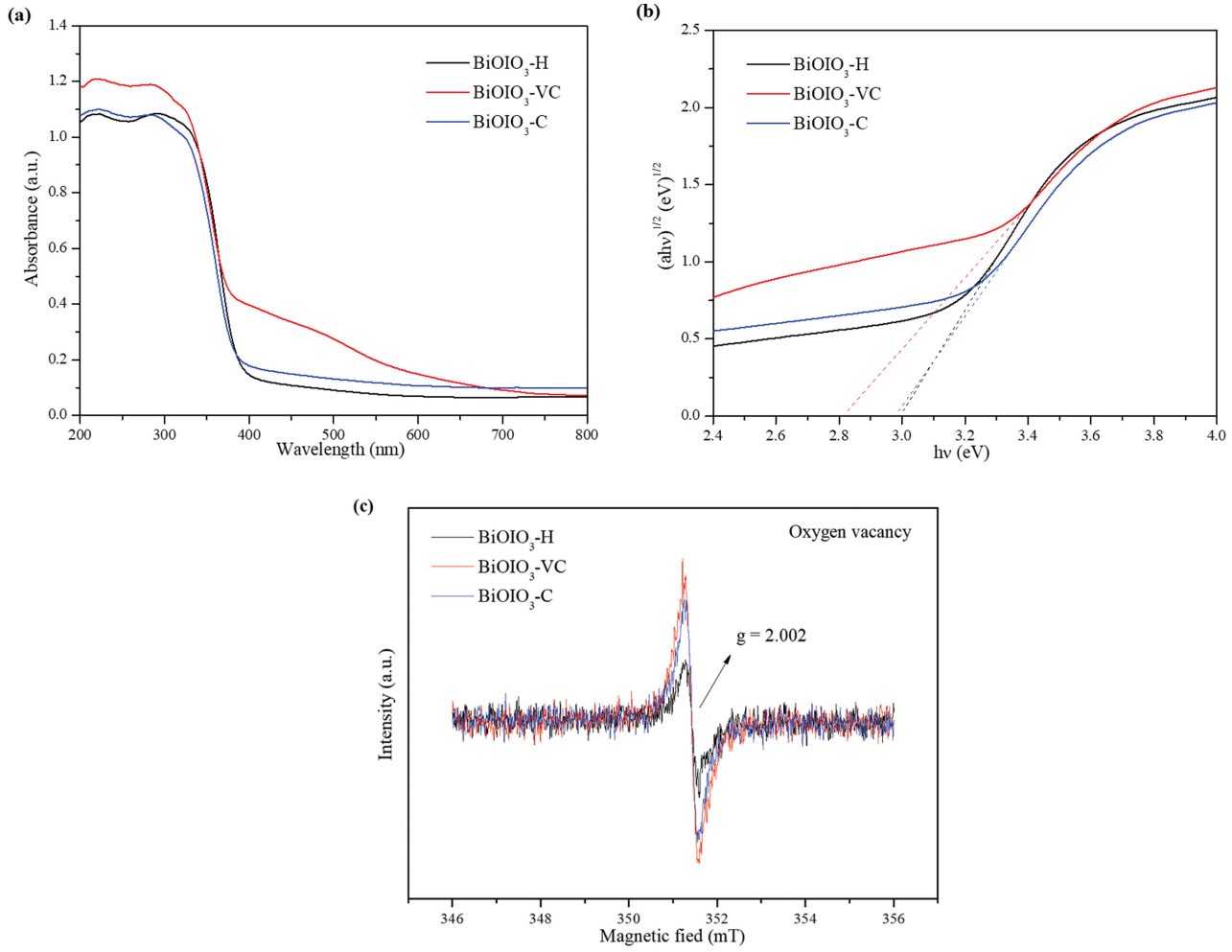

Fig. 6. (a) UV-vis DRS; (b) $(\alpha h\nu)^{1/2}$ versus $(h\nu)$ plot; (c) EPR spectra.

From the UV-vis spectra (Fig. 6(a)) and the associated $(\alpha h\nu)^{1/2}$ versus $(h\nu)$ plot (Fig. 6(b)), both $BiOIO_3$-H and $BiOIO_3$-C have strong absorption of ultraviolet light, but weak to visible light, indicating that direct calcination has no significant improvement in visible light absorption of $BiOIO_3$. Approximate horizontal lines in visible light region imply uniform reflection of incident light, so the color of $BiOIO_3$-H and $BiOIO_3$-C is both white. The light absorption of $BiOIO_3$-VC is uniformly improved in the range of 200-800 nm (compared with $BiOIO_3$-H), and remarkably, it absorbs a large amount of blue-violet light in the visible light range. However, absorption is still weak for red light with a longer wavelength, so that the reflection is strong, which is why the sample appears pink.

Electron paramagnetic resonance (EPR) is based on the magnetic moment of unpaired electrons, which can be used to detect the unpaired electrons contained in atoms or molecules of substances. From Fig. 6(c), the g factor, which reflects the interaction between the electron spin motion and the orbital motion, has a value of 2.002, corresponding to the characteristics of oxygen vacancy [37]. It can be found that the EPR response of sample $BiOIO_3$-H is relatively weak, while the EPR response of $BiOIO_3$ after vacuum calcination ($BiOIO_3$-VC) is significantly improved, with the peak strength nearly three-times that of the original. This indicates that vacuum calcination can significantly increase the oxygen vacancy concentration of $BiOIO_3$, which is well consistent with the above analysis.

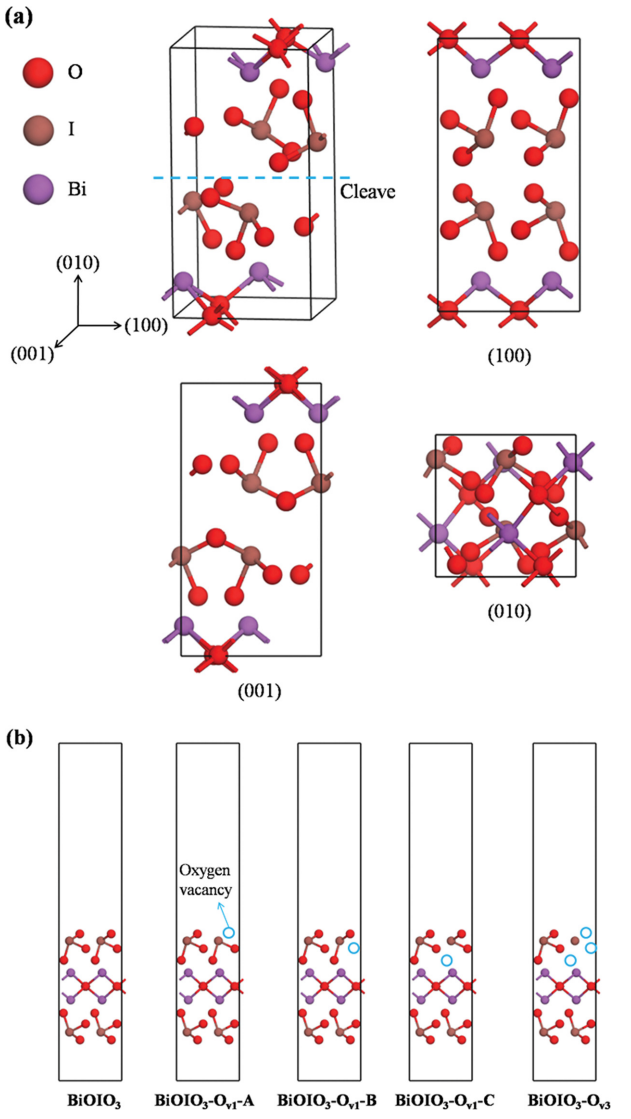

Fig. 7. (a) Crystal cell model of $BiOIO_3$; (b) $BiOIO_3$ (010) surface with/without oxygen vacancy.

In addition, a density functional theory (DFT) calculation was carried out to further support the above assumption. The crystal cell model of $BiOIO_3$ is shown in Fig. 7(a), which has a typical Aurivillius-type layered structure [20]. The nanosheet $BiOIO_3$ is composed of $(Bi_2O_2)^{2+}$ layer as skeleton, with $(IO_3)^-$ layers hanging on both sides, which has significant macroscopic polarization characteristics. The iodate layers between the two (010) facets interact with each other by van der Waals forces, so this surface is easier to cleave and peel off. Dai et al. [38] cleverly constructed a vertical BiOI/$BiOIO_3$ heterojunction based on the (010) surface of $BiOIO_3$, showing stronger photocatalytic performance. Therefore, in this paper, the (010) plane of $BiOIO_3$ was selected as the representative crystal plane to be segmented and exposed to form a surface, as shown in Fig. 7(b). A vacuum layer of 10 Å was cited to avoid the influence of the existence of adjacent layers on the conclusion [39,40]. Considering that there are three kinds of oxygen atoms in different environments in one $(IO_3)^-$ ion, three Nanosheet $BiOIO_3$ model with one oxygen vacancy were constructed, named as $BiOIO_3$-O_{v1}-A, $BiOIO_3$-O_{v1}-B and $BiOIO_3$-O_{v1}-C (where v1 represents an oxygen vacancy). The structure of an $(IO_3)^-$ ion losing all its oxygen that exposing exposed iodine was also calculated, which was named as $BiOIO_3$-O_{v3}. After the geometrical optimization of the above structure, the related energy calculation was carried out on this basis.

The band structure and density of states (DOS) analysis of $BiOIO_3$ with and without oxygen vacancy are shown in Fig. 8. When the surface of $BiOIO_3$ nanosheets is intact without oxygen vacancy defects, the band gap energy (E_{bg}) is 2.692 eV (Fig. 8(a)). This value is underestimated to some extent, compared with the experimental value (~3 eV in this paper). This is due to the inherent error caused by the GGA/PBE functional evaluation of the semiconductor band gap [30]. Therefore, the absolute value of the band gap calculated by DFT is only for reference, but the change of its relative value is of significance for analysis. As the complete $BiOIO_3$ without any defects, the valence band (VB) and conduction band (CB) are formed by the contribution of p orbitals, hybridized with a small number of s orbitals. There is no energy level distribution between the valence band maximum (VBM) and conduction band minimum (CBM), which presents a strictly forbidden band. However, when there is an oxygen vacancy on the surface of $BiOIO_3$ nanosheets, the band gap is significantly shortened, reaching the range of 1.015-1.308 eV (Fig. 8(b)-(d)). It can be found that there is a discrete p orbital at the Fermi level, showing a semi-filled band structure. While, when the oxygen vacancy concentration further increases, the original $(IO_3)^-$ only remains an exposed iodine atom, resulting in a local point-like zero-dimensional BiOI structure, with the band gap almost disappearing to 0.261 eV. Moreover, a wide and rich band distribution appears in the original band gap posi-

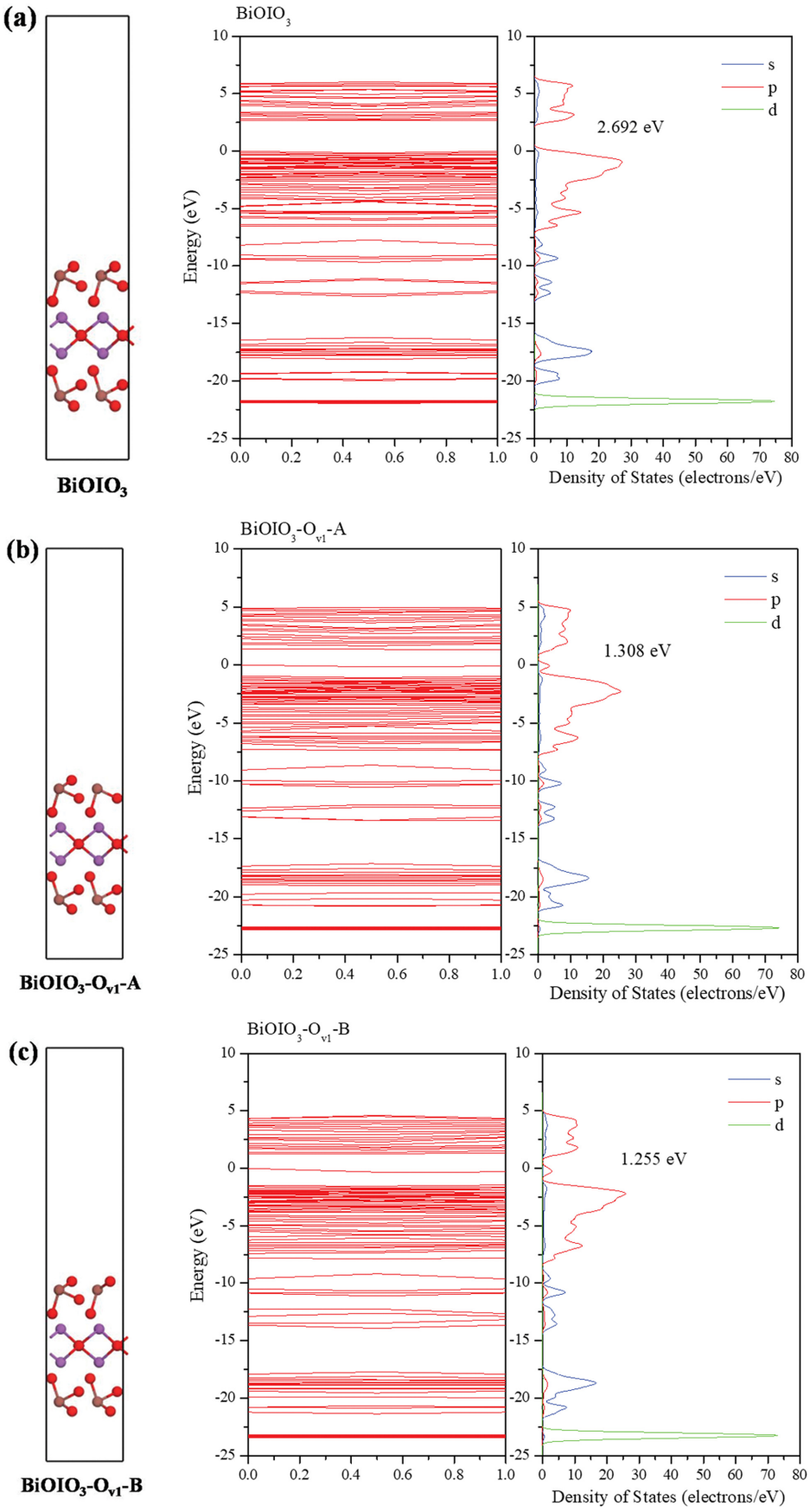

Fig. 8. Band structure and density of states analysis: (a) $BiOIO_3$; (b) $BiOIO_3$-O_{v1}-A; (c) $BiOIO_3$-O_{v1}-B; (d) $BiOIO_3$-O_{v1}-C; (e) $BiOIO_3$-O_{v3}.

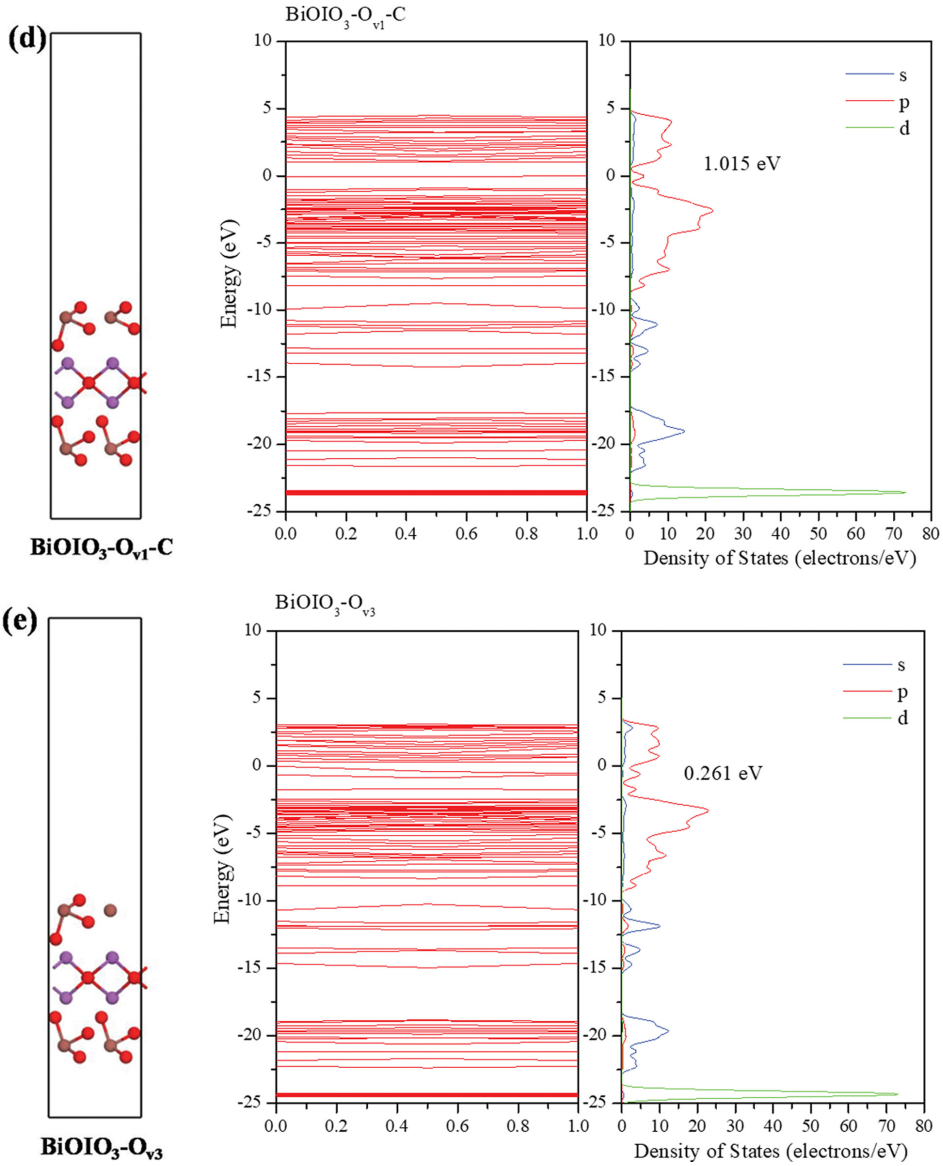

Fig. 8. Continued.

tion. It can be seen that when oxygen vacancies are formed on the surface of $BiOIO_3$ nanosheets, the band gap width will be significantly reduced. Depending on the number of oxygen vacancies, a local BiOI structure may form. However, the characteristic peak of BiOI is not observed in the XRD spectrum, since there are no blocks of BiOI produced.

Shown in Fig. 9 is the absorption spectrogram achieved by DFT calculation. It can be seen that the intact $BiOIO_3$ without oxygen vacancy relatively easily absorbs ultraviolet light, but almost no absorption for long wavelengths light. Poor absorption, in other words, strong reflection, so pure $BiOIO_3$ macroscopically appears white. With the formation of oxygen vacancy, the absorption to the incident light in the visible light range is enhanced to varying degrees, while the absorption of blue violet light is more enhanced. The calculation results of DFT are in good agreement with the experimental data, which verifies the feasibility of the above conjecture.

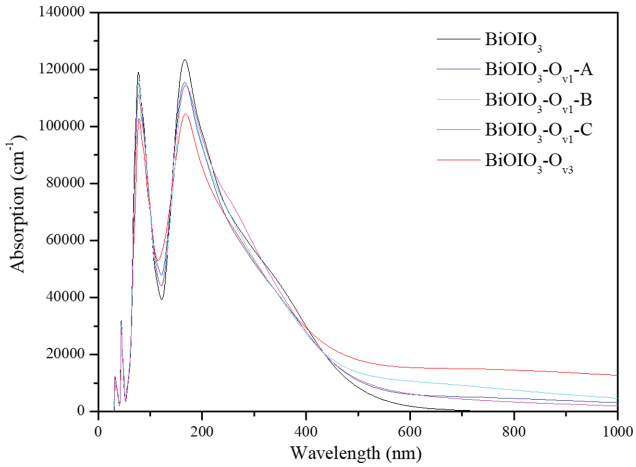

Fig. 9. Absorption spectrogram achieved by DFT calculation.

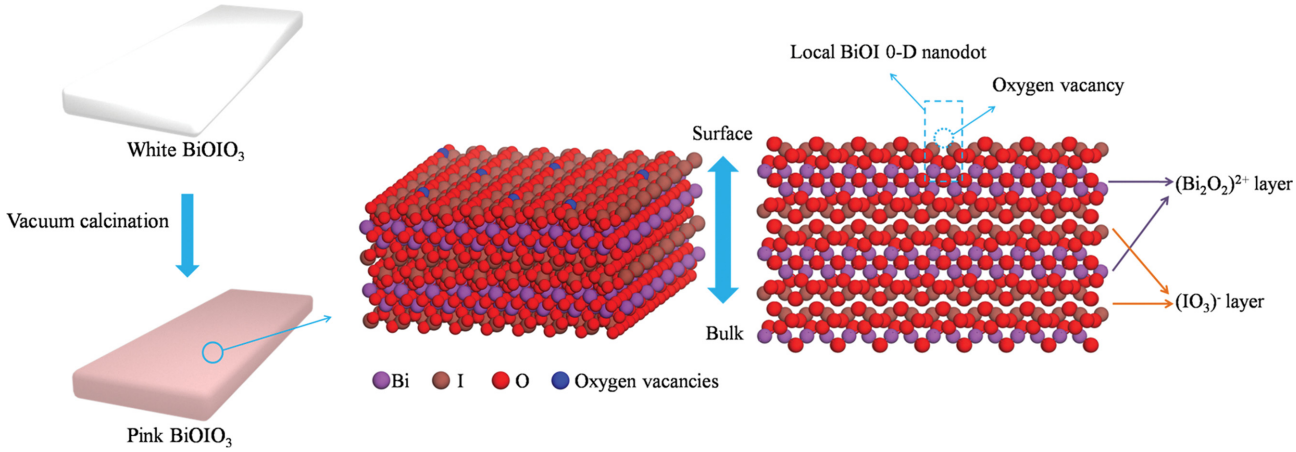

Fig. 10. Schematic diagram for the photocatalytic performance improvement of pink $BiOIO_3$.

Through the above experimental analysis and theoretical calculation, the following photocatalytic performance improvement mechanism can be given, as shown in Fig. 10. First, the pure $BiOIO_3$, with a large band gap, only shows a strong absorption of ultraviolet light, while the absorption of visible light range is weak with uniform reflection and appearing white. After the treatment of vacuum calcination, due to the influence of the external environment of vacuum degree, the crystal surface structure of $BiOIO_3$ has changed. The partial loss of surface lattice oxygen in $BiOIO_3$ crystals resulted in the formation of point-like BIOI morphology and the formation of BIOI/$BiOIO_3$ heterojunction with intact $BiOIO_3$, resulting in a significant decrease in band gap and improved light absorption within the visible light range. In addition, the light absorption enhancement of short wavelength is more intense, while the light absorption enhancement of long wave band is not obvious, so the sample appears pink macroscopically. An oxygen vacancy is formed on the surface discretely so that no large chunks of BIOI crystals are formed, so the characteristic peak of BIOI is not observed in the XRD image. Note that vacuum calcination leads to a significant increase in the specific surface area of the sample, which is also conducive to the adsorption of reactants, thus indirectly improving the efficiency of mercury removal.

CONCLUSIONS

Pink $BiOIO_3$ nanosheets were successfully synthesized via vacuum calcination. The spatial layout of $BiOIO_3$ nanosheets changed, reducing the agglomeration and becoming more fluffy and rich in pores, with the specific surface area remarkably increased by 50.4% (29.60→44.52 m^2/g). The in-situ exposure of I^- ions on sample surface resulted in rich oxygen vacancies and shortening the band gap, which is conducive to the absorption of visible light. The formed local BiOI Zero-dimensional nanodots provide heterojunction-like effect combined with the $BiOIO_3$, thus obtaining improved photocatalytic performance.

ACKNOWLEDGEMENTS

This work was partially sponsored by National Natural Science Foundation of China (52076126) and Natural Science Foundation of Shanghai (18ZR1416200), and Projects of Shanghai Science and Technology Committee (20DZ1205207).

SUPPORTING INFORMATION

Additional information as noted in the text. This information is available via the Internet at http://www.springer.com/chemistry/journal/11814.

REFERENCES

1. K. Balasundaram and M. Sharma, *Crit. Rev. Env. Sci. Tec.*, **49**, 1700 (2019).
2. Z. Qi, J. Li, D. Wu, W. Xie, X. Li and C. Liu, *Energy Fuels*, **31**, 1741 (2017).
3. X. Li, C. Zhou, J. Li, S. Lu and J. Yan, *Environ. Sci. Pollut. Res. Int.*, **26**, 12798 (2019).
4. T. Czech, A. Marchewicz, A. T. Sobczyk, A. Krupa, A. Jaworek, Ł. Śliwiński and D. Rosiak, *Process Saf. Environ. Prot.*, **133**, 18 (2020).
5. A. B. Mukherjee, R. Zevenhoven, P. Bhattacharya, K. S. Sajwan and R. Kikuchi, *Resour. Conserv. Recycl.*, **52**, 571 (2008).
6. S. Sjostrom, M. Durham, C. J. Bustard and C. Martin, *Fuel*, **89**, 1320 (2010).
7. W. Zhao, X. Geng, J. Lu, Y. Duan, S. Liu, P. Hu, Y. Xu, Y. Huang, J. Tao and X. Gu, *Fuel*, **285**, 119131 (2021).
8. T. Huang, Y. Duan, Z. Luo, S. Zhao, X. Geng, Y. Xu, Y. Huang, H. Wei, S. Ren, H. Wang and X. Gu, *Ind. Eng. Chem. Res.*, **58**, 15553 (2019).
9. H. Wang, S. Zhou, L. Xiao, Y. Wang, Y. Liu and Z. Wu, *Catal. Today*, **175**, 202 (2011).
10. H. Park, Y. Park, W. Kim and W. Choi, *J. Photoch. Photobio. C.*, **15**, 1 (2013).
11. C. Wang, W. Wang, H. Fan, N. Zhao, J. Ma, M. Zhang and A. K. Yadav, *ACS Appl. Mater. Interfaces*, **12**, 5234 (2020).
12. K. Ozawa, M. Emori, S. Yamamoto, R. Yukawa, S. Yamamoto, R. Hobara, K. Fujikawa, H. Sakama and I. Matsuda, *J. Phys. Chem. Lett.*, **5**, 1953 (2014).
13. L. Hu, S. Dong, Q. Li, J. Feng, Y. Pi, M. Liu, J. Sun and J. Sun, *J.*

Alloys Compd., **633**, 256 (2015).
14. J. Jia, P. Xue, R. Wang, X. Bai, X. Hu, J. Fan and E. Liu, *J. Chem. Technol. Biotechnol.*, **93**, 2988 (2018).
15. J. Fan, X. Hu, Z. Xie, K. Zhang and J. Wang, *Chem. Eng. J.*, **179**, 44 (2012).
16. X. Lin, F. Huang, W. Wang, Z. Shan and J. Shi, *Dyes. Pigm.*, **78**, 39 (2008).
17. Y. Sun, Z. Zhao, W. Zhang, C. Gao, Y. Zhang and F. Dong, *J. Colloid. Interface Sci.*, **485**, 1 (2017).
18. R. He, D. Xu, B. Cheng, J. Yu and W. Ho, *Nanoscale Horiz.*, **3**, 464 (2018).
19. D. Liu, W. Yao, J. Wang, Y. Liu, M. Zhang and Y. Zhu, *Appl. Catal. B*, **172-173**, 100 (2015).
20. S. D. Nguyen, J. Yeon, S. H. Kim and P. S. Halasyamani, *J. Am. Chem. Soc.*, **133**, 12422 (2011).
21. F. Chen, H. Huang, L. Ye, T. Zhang, Y. Zhang, X. Han and T. Ma, *Adv. Funct. Mater.*, **28**, 1 (2018).
22. J. Feng, H. Huang, S. Yu, F. Dong and Y. Zhang, *Phys. Chem. Chem. Phys.*, **18**, 7851 (2016).
23. Y. Su, L. Zhang and W. Z. Wang, *Int. J. Hydrog.*, **41**, 10170 (2016).
24. J. Xie, Y. Cao, J. Hu, Y. Tang and D. Jia, *Green Chem.*, **22**, 1424 (2020).
25. X. Zhang, D. Wang, X. Man, J. Wu, Q. Liu, Y. Qi, Z. Liu, X. Zhao, J. Wu and C. Hao, *J. Colloid. Interface Sci.*, **558**, 123 (2020).
26. H. Huang, S. Tu, C. Zeng, T. Zhang, A. H. Reshak and Y. Zhang, *Angew. Chem. Int. Ed. Engl.*, **56**, 11860 (2017).
27. X. M. Qi, M. L. Gu, X. Y. Zhu, J. Wu, H. M. Long, K. He and Q. Wu, *Chem. Eng. J.*, **285**, 11 (2016).
28. X. Sun, J. Wu, Q. Li, Q. Liu, Y. Qi, L. You, Z. Ji, P. He, P. Sheng, J. Ren, W. Zhang, J. Lu and J. Zhang, *Appl. Catal. B*, **218**, 80 (2017).
29. Y. Ling, J. Wu, X. Man, Y. Xu, Q. Liu, Y. Qi, Q. Wu, X. Qi, T. Jia and Z. Guo, *Mater. Res. Bull.*, **122**, 110620 (2020).
30. M. Ernzerhof and J. P. Perdew, *J. Chem. Phys.*, **109**, 3313 (1998).
31. R. Zhou, J. Wu, J. Zhang, H. Tian, P. Liang, T. Zeng, P. Lu, J. Ren, T. Huang, X. Zhou and P. Sheng, *Appl. Catal. B*, **204**, 465 (2017).
32. J. Wu, K. Xu, Q. Liu, Z. Ji, C. Qu, X. Qi, H. Zhang, Y. Guan, P. He and L. Zhu, *Appl. Catal. B*, **232**, 135 (2018).
33. D. Cui, Y. Zheng and X. Song, *J. Exp. Nanosci.*, **11**, 1000 (2016).
34. W. Wang, B. Huang, X. Ma, Z. Wang, X. Qin, X. Zhang, Y. Dai and M. H. Whangbo, *Chem. Eur. J.*, **19**, 14777 (2013).
35. X. Zhou, J. Wu, Q. Li, T. Zeng, Z. Ji, P. He, W. Pan, X. Qi, C. Wang and P. Liang, *J. Mol. Catal.*, **355**, 26 (2017).
36. Y. Sun, T. Xiong, F. Dong, H. Huang and W. Cen, *Chem. Commun. (Camb.)*, **52**, 8243 (2016).
37. H. Wang, D. Yong, S. Chen, S. Jiang, X. Zhang, W. Shao, Q. Zhang, W. Yan, B. Pan and Y. Xie, *J. Am. Chem. Soc.*, **140**, 1760 (2018).
38. W. Dai and Z. Zhao, *Phys. Chem. Chem. Phys.*, **19**, 9900 (2017).
39. L. Liu, Q. Deng, C. Zheng, S. Wang, J. Wang and X. Gao, *Aerosol Air Qual. Res.*, **19**, 2320 (2019).
40. J. Xing, C. Wang, C. Zou and Y. Zhang, *Appl. Surf. Sci.*, **510**, 145488 (2020).

Supporting Information

Enhanced photocatalytic activity on elemental mercury over pink $BiOIO_3$ nanosheets with abundant oxygen vacancies

Yang Ling[*,‡], Jiachen Li[,‡], Jiang Wu[*,**,†], Hailong Liu[**], Xu Mao[**], Yongfeng Qi[***], Qian Ma[**], Qizhen Liu[****,†], Zhanwei Qiao[**], and Weiqun Chu[**]**

*School of Energy and Power Engineering, University of Shanghai for Science and Technology, Shanghai 200093, China
**College of Energy and Mechanical Engineering, Shanghai University of Electric Power, Shanghai 200090, China
***School of Hydraulic Energy and Power Engineering, Yangzhou University, Yangzhou 225127, China
****Shanghai Environment Monitoring Center, Shanghai 200030, China
(*Received 17 May 2021 • Revised 4 August 2021 • Accepted 12 August 2021*)

Photocatalytic Oxidation of Elemental Mercury

The as-prepared samples were tested by photocatalytic oxidation of gaseous elemental mercury (Hg^0), and the experiment bench was shown in Fig. S1, the nitrogen flow was divided into two branches, one streamed with 1 L/min flow rates and the other one with 0.2 L/min flow rates. The 0.2 L/min flow rates line passed through a mercury generator (PSA, UK). Then the two streams were uniformly mixed in a mixing tank, providing stable Hg^0 vapor (about 60 μg/m^3 in this work). The Hg^0 concentration was measured by mercury analyzer (RA-915-M, Lumex, Russia).

In each test, 30 mg as-prepared photocatalyst was loaded evenly on a quartz glass, under 9W LED light (with filter λ>400 nm). The elemental mercury (Hg^0) removal efficiency of as-prepared samples under visible light could be calculated via Eqs. (1):

$$\eta = \frac{[Hg^0]_{in} - [Hg^0]_{out}}{[Hg^0]_{in}} \times 100\% \quad (1)$$

where $[Hg^0]_{in}$ represents the Hg^0 concentration (μg/m^3) at the reactor inlet, while $[Hg^0]_{out}$ represents the Hg^0 concentration (μg/m^3) at the reactor outlet.

Photocatalytic Degradation of Rhodamine B

Fig. S2(a) is the experimental setting of photocatalytic degradation of RhB, and in each test, 100 ml of 10 mg/L RhB solution was used and 50 mg catalyst sample was dispersed in the solution. After 30 min of darkness, the visible light lamp was turned on for photocatalytic reaction. After 15, 30, 45, 60 and 90 min of reaction, 3 ml of supernatant was extracted by a syringe with filter. The supernatant was then transferred to a liquid-phase UV-vis spectrophotometer, and the absorbance data were obtained under the irradiation of monochromatic light with 552 nm wavelength. According to the formula A=K*L*C, where A is the absorbance of the liquid under test, K is a proportional coefficient, L is the optical path length of the cuvette in the UV-vis spectrophotometer (the value is 10 mm in this work), and C is the concentration of RhB in the liquid under test. At the beginning of the experiment, RhB solution with known concentration were taken for UV-vis test, and then, the standard curve was drawn as shown in Fig. S2(b). The curve has a good linear relationship, and the subsequent RhB concentration is calculated from this fitting curve.

The experimental results of photocatalytic degradation of RhB

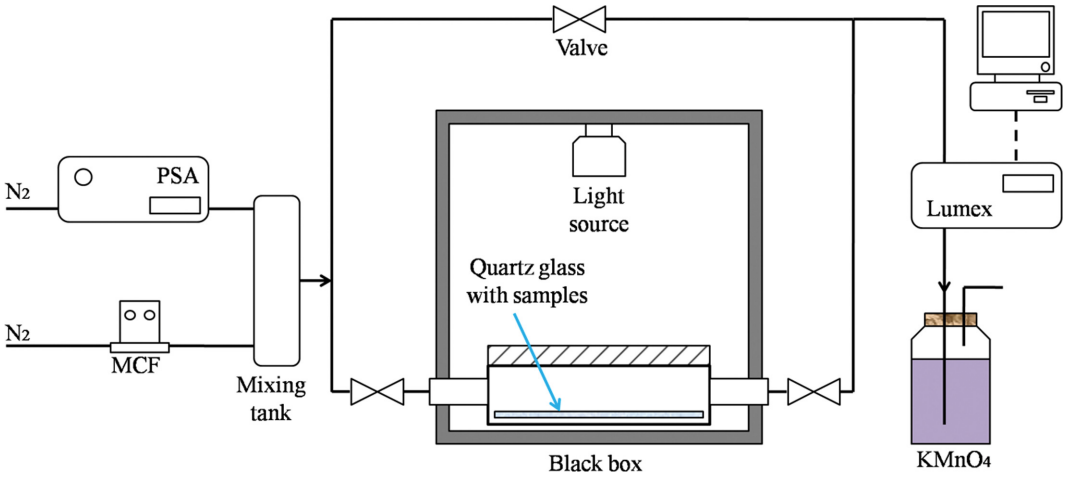

Fig. S1. Schematic diagram of the experimental system.

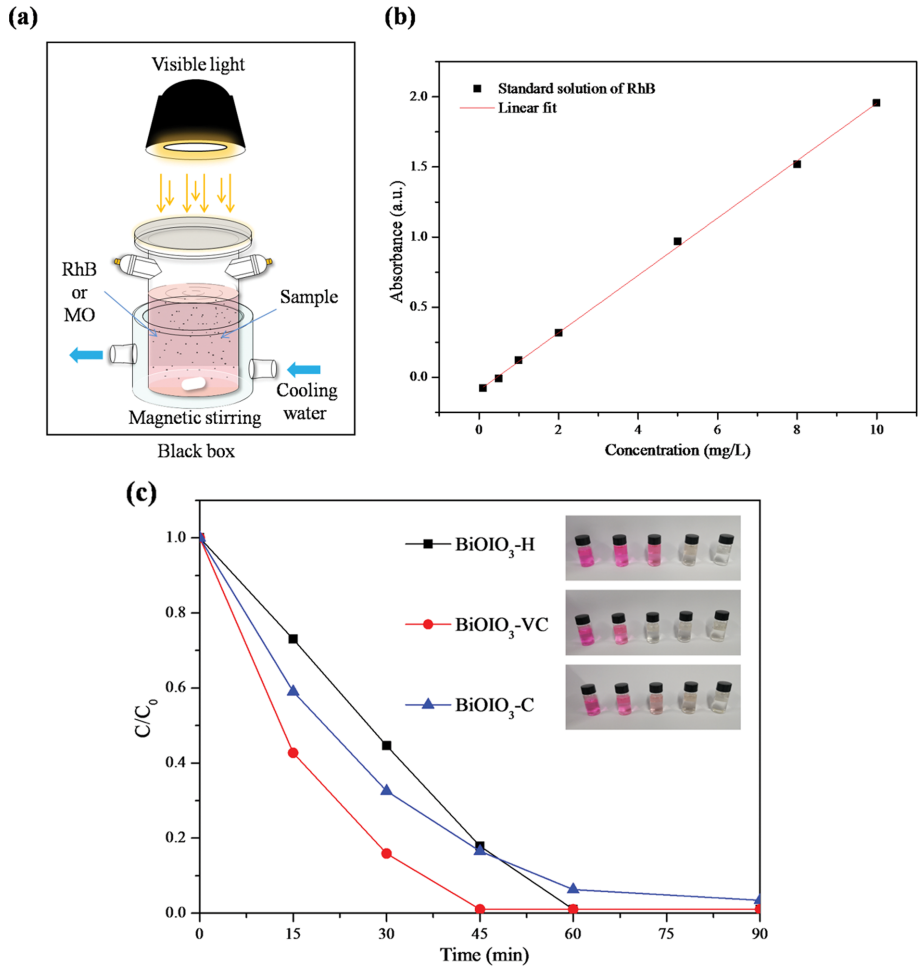

Fig. S2. (a) Experimental setup for photocatalytic degradation of RhB; (b) Standard curve of absorbance versus concentration; (c) Photocatalytic degradation efficiency of the as-prepared samples.

via the as-prepared samples in this paper are shown in Fig. S2(c). The catalytic performance is characterized by C/C_0, where C_0 is the initial concentration of RhB solution (10 mg/L), and C is the RhB concentration at the current moment. It can be seen that among the three samples, the performance of $BiOIO_3$-H is poor, which takes 60 min to basically complete the degradation of RhB. While, the performance of the $BiOIO_3$-C is in between. $BiOIO_3$-VC has the best performance: At the beginning of the reaction, RhB concentration drops rapidly. After 15 min, nearly 60% of RhB is degraded, and after 45 min, the degradation is complete. Therefore, vacuum calcination can effectively improve the photocatalytic performance of $BiOIO_3$.

Adsorption Site of Mercury

In order to explore the active point sites of mercury adsorption, the supplementary DFT calculation was carried out, and the results are shown in Fig. S3. The yellow, green and blue spheres in Fig. S3(a) indicate three potential adsorption sites, namely, the iodine top site (I_T), the oxygen top site (O_T), and the hollow site (H), respectively. The mercury atoms were placed in the above mentioned adsorption sites of structure $BiOIO_3$, $BiOIO_3$-O_{v1}-A, $BiOIO_3$-O_{v1}-B, $BiOIO_3$-O_{v1}-C and $BiOIO_3$-O_{v3}, successively, and then the geometric optimization was performed. The adsorption energy is calculated as $E_{ad}=E_{sys}-E_{surf}-E_{Hg}$, where E_{sys} is the total energy of the stable system formed after adsorption, E_{surf} is the total energy of the surface before adsorption, and E_{Hg} is the total energy of an isolated elemental mercury. The negative adsorption energy indicates that the adsorption structure is stable, and the larger the absolute value is, the more stable it is.

The adsorption energy of all structures are shown in Fig. S3(b). It can be seen that when mercury is adsorbed on the intact $BiOIO_3$ surface without any defects, the adsorption energy is in the range of −0.188~−0.173 eV, and the best adsorption position is at the iodine top site. The situation is different when the oxygen vacancy concentration is low that the iodate group loses only one oxygen atom. The optimal adsorption energies of mercury on structures $BiOIO_3$-O_{v1}-A and $BiOIO_3$-O_{v1}-B are as low as −0.206 eV and −0.203 eV, which is slightly better than that on the surface without defects. While, the adsorption energy of mercury on structure $BiOIO_3$-O_{v1}-C is in the range of −0.172~−0.168 eV, and the adsorption performance is not improved significantly. This is because in structure $BiOIO_3$-O_{v1}-A and $BiOIO_3$-O_{v1}-B, oxygen vacancies occur on the surface. While in structure $BiOIO_3$-O_{v1}-C, oxygen vacancies occur on the sub-surface, close to the inside of the crystal block, so the promotion of mercury adsorption is not obvious here. When

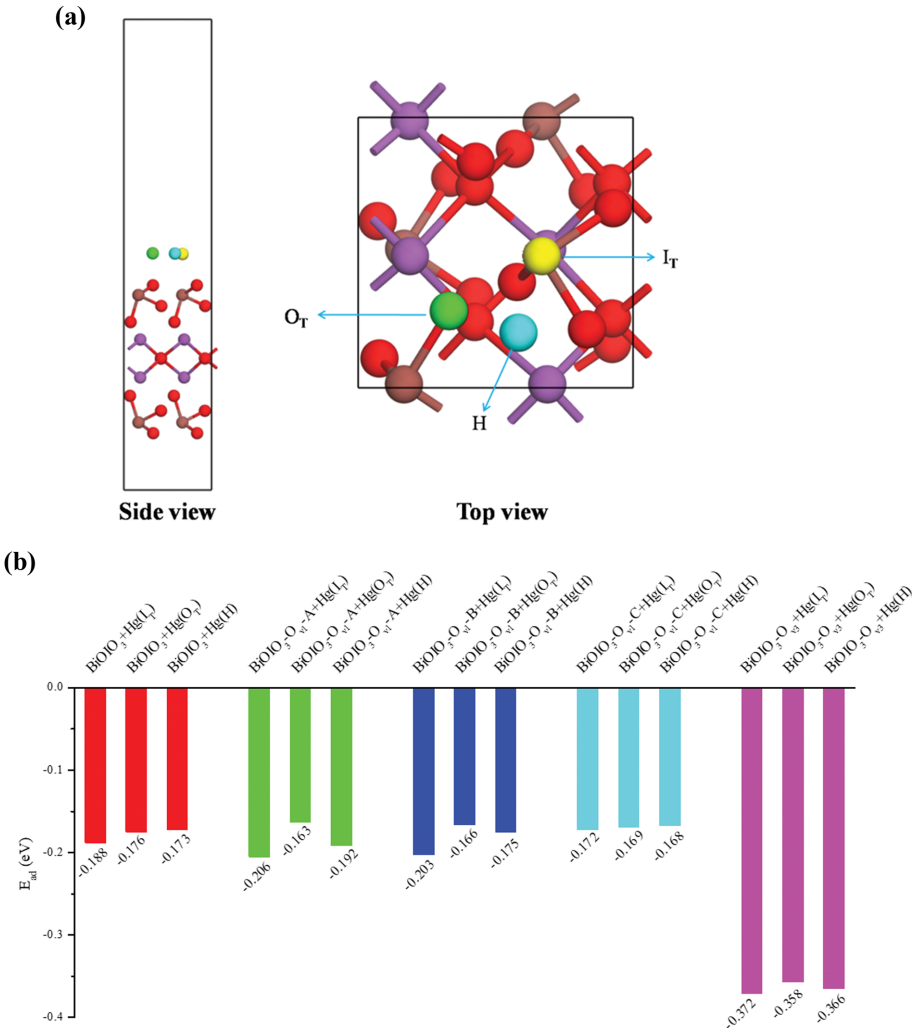

Fig. S3. (a) Potential sites for mercury adsorption; (b) Adsorption energy.

the oxygen vacancy concentration is further increased, the adsorption energy of structure $BiOIO_3$-O_{v3} for mercury is significantly increased to −0.372~−0.358 eV, which is almost twice that of the intact surface. The adsorption energy is related to the oxygen vacancy concentration and its formation position. It can be inferred from the above analysis that the catalytic reaction tend to take place at the oxygen vacancy defects on the catalyst surface.